Probing neuronal activation by functional quantitative susceptibility mapping under a visual paradigm: A group level comparison with BOLD fMRI and PET

Özbay, Pinar Senay ; Warnock, Geoffrey ; Rossi, Cristina ; Kuhn, Felix ; Akin, Burak ; Pruessmann, Klaas Paul ; Nanz, Daniel

DOI: https://doi.org/10.1016/j.neuroimage.2016.05.013

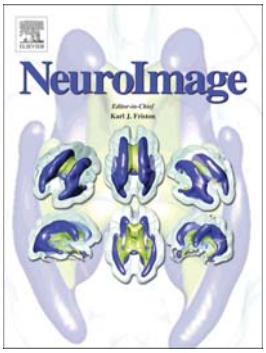

Probing neuronal activation by functional quantitative susceptibility mapping under a visual paradigm: A group level comparison with BOLD fMRI and PET

Pinar Senay Özbay, Geoffrey Warnock, Cristina Rossi, Felix Kuhn, Burak Akin, Klaas Paul Pruessmann, Daniel Nanz

PII: S1053-8119(16)30124-0
DOI: doi: 10.1016/j.neuroimage.2016.05.013
Reference: YNIMG 13170

To appear in: *NeuroImage*

Received date: 15 January 2016
Revised date: 2 May 2016
Accepted date: 3 May 2016

Please cite this article as: Özbay, Pinar Senay, Warnock, Geoffrey, Rossi, Cristina, Kuhn, Felix, Akin, Burak, Pruessmann, Klaas Paul, Nanz, Daniel, Probing neuronal activation by functional quantitative susceptibility mapping under a visual paradigm: A group level comparison with BOLD fMRI and PET, *NeuroImage* (2016), doi: 10.1016/j.neuroimage.2016.05.013

Probing neuronal activation by functional quantitative susc eptibility mapping under a visual paradigm: a group level comparison with BOLD fMRI and PET

Pinar Senay Özbay[a, b], Geoffrey Warnock[c, d], Cristina Rossi[a], Felix Kuhn[d], Burak Akin[e], Klaas Paul Pruessmann[b], and Daniel Nanz[a]

[a] Institute of Diagnostic and Interventional Radiology, University Hospital Zurich and University of Zurich, Zurich, Switzerland

[b] Institute for Biomedical Engineering, University of Zurich and ETH Zurich, Switzerland

[c] PMOD Technologies Ltd., Zurich, Switzerland

[d] Department of Nuclear Medicine, University Hospital Zürich and University of Zurich, Zurich, Switzerland

[e] Medical Physics, University Medical Center, Freiburg, Germany

To be submitted to Neuroimage as regular article

Corresponding author
P. S. Özbay
Universitätsspital Zürich
Institut für Diagnostische und Interventionelle Radiologie
Rämistrasse 100
8091 Zürich
Phone: +41 (0) 44 255 2900
Email: Pinar.Oezbay@usz.ch

ABSTRACT

Dynamic changes of brain-tissue magnetic susceptibility provide the basis for functional MR imaging (fMRI) via T2*-weighted signal-intensity modulations. Promising initial work on a detection of neuronal activity via quantitative susceptibility mapping (fQSM) has been published but consistently reported on ill-understood positive and negative activation patterns (Balla et al., 2014; Chen and Calhoun, 2015a). We set out to (i) demonstrate that fQSM can exploit established fMRI data acquisition and processing methods and to (ii) better describe aspects of the apparent activation patterns using fMRI and PET as standards of reference. Under a standardized visual-stimulation paradigm PET and 3-T gradient-echo EPI-based fQSM, fMRI data from 9 healthy volunteers were acquired and analyzed by means of Independent Component Analysis (ICA) at subject level and, for the first time, at group level. Numbers of activated (z-score > 2.0) voxels were counted and their mean z-scores calculated in volumes of interest (occipital lobe ($N_{\mathrm{occ\_lobe}}$), segmented occipital grey-matter ($N_{\mathrm{GM\_occ\_lobe}}$), large veins (N_{veins})), and in occipital-lobe voxels commonly activated in fQSM and fMRI component maps. Common but not entirely congruent regions of apparent activation were found in the occipital lobe in *z-score* maps from all modalities, fQSM, fMRI and PET, with distinct BOLD-negatively correlated regions in fQSM data. At subject-level, N_{occ_lobe}, $N_{GM\_occ\_lobe}$ and their mean z-scores were significantly smaller in fQSM than in fMRI, but their ratio, $N_{GM\_occ\_lobe}$ / N_{occ_lobe}, was comparable. N_{veins} did not statistically differ and the ratio $N_{\mathrm{veins}}/N_{GM\_occ\_lobe}$ as well as the mean z-scores were higher for fQSM than for fMRI. In veins and immediate vicinity, z-score maps derived from both phase and fQSM-data showed positive and negative lobes resembling dipole shapes in simulated field and phase maps with no correlate in fMRI or PET data. Our results show that standard fMRI tools can directly be used for fQSM processing, and suggest that fQSM may have the potential to detect grey-matter activation distant from large veins, to improve detection of veins with stimulus-induced venous oxygen saturation (SvO2) variations, and to better localize areas of activation. However, our

results seem to clearly expose issues that phenomenologically resemble an incomplete dipolar inversion and that need to be subject to further investigation.

Keywords: fMRI, BOLD, susceptibility, quantitative susceptibility mapping (QSM), fQSM, phase, independent component analysis (ICA), visual paradigm

1. INTRODUCTION

Functional MRI (fMRI) detects neuronal activity via changes of oxygen-saturation levels caused by variations of regional blood and oxygen supply in relation to the metabolic oxygen consumption rate. Conventional Blood-Oxygenation-Level-Dependent (BOLD) fMRI exploits the magnitude of the MR signal, whose changes are dominated by differences in the magnetic susceptibility between blood samples at different levels of oxygen saturation (Blockley et al., 2013). Variations of the signal magnitude represent, however, an indirect measure of the underlying susceptibility changes and recent studies demonstrated some of the problematic aspects of the signal-intensity-based approach, such as a response that does not linearly vary with tissue oxygenation or problems associated with the non-negativity of the magnitude information (Chen and Calhoun, 2015b; Chen and Calhoun, 2011).

Functional susceptibility mapping, fQSM, potentially offers a more direct measure of susceptibility changes and, thus, of activation-induced variations of oxygen saturation, but it requires analysis of signal phase. The often discarded phase of the MR signal has been shown (Arja et al., 2010) to hold additional information, in part complementary to that from magnitude data. However, it is not readily accessible, due to (i) extra-cerebral non-local field-source interference causing brain-tissue signal phase to change with (a) long-term drifts of the static magnetic field generated by the acquisition hardware or with (b) periodic displacement of thoracic anatomy during the respiratory and cardiac cycles, and due to (ii) the restriction of phase values to the interval]-□, □], which causes numerous phase wraps for the long echo times required for optimum sensitivity in fMRI. Both, signal phase and magnitude in T2*-weighted data may also be critically distorted by intra-cerebral non-local field-source interference (Turner, 2002): e.g., phase as well as T2*-variations in a brain-tissue voxel may wrongly be assumed to reflect intra-voxel physiological changes while they might only reflect oxygen-saturation changes of blood in a nearby larger vein (Turner, 2002). Techniques of quantitative susceptibility mapping (QSM) promises to capitalize on the phase-data information, while alleviating extra-cerebral non-local

field-source interference, mostly by dedicated phase pre-processing, and extracting intra-cerebral non-local field-source interference, via the–albeit ill-defined–conversion of measured 3D field distribution to 3D magnetic susceptibility distribution by dipolar inversion (Schweser et al., 2013; Shmueli et al., 2009). Functional QSM, fQSM (Balla et al., 2014), promises several advantages, beyond information potentially complementary to fMRI: it is based on a quantity that, compared to T2*-weighted signal magnitude, less strongly depends on experimental details, e.g., magnet shimming, may vary mostly linearly with tissue oxygenation (Fan et al., 2016; Wehrli et al., 2016) and may hypothetically offer better localization of neuronal activity. It also less strongly depends on data-acquisition sequence (Sun and Wilman, 2015) and parameters and should be better reproducible across scanners from different manufacturers and field strengths (Deh et al., 2015). While recent studies confirmed a considerable potential of fQSM (Balla et al., 2014; Bianciardi et al., 2014; Chen and Calhoun, 2015a), they quite consistently reported on apparent activation that negatively correlated with the stimulus, often in tissue volumes of predominantly positive correlation in fMRI, an effect that is only poorly understood. In this study, we aimed to exploratively validate fQSM with data from a clinical 3T MR scanner and healthy volunteers, to propose a straightforward pipeline for fQSM analyses, and to focus on the phenomenology of volumes with negative correlations. Results from simultaneously acquired fMRI data, from truly quantitative cerebral blood flow (CBF) maps from Position Emission Tomography (PET) (Fox et al., 1984), and simulated data served as standards of reference. Preliminary results have been presented as conference and workshop abstracts (Özbay et al., 2015a; Özbay et al., 2014a; Özbay et al., 2014c).

2. MATERIALS AND METHODS

2.1 VOLUNTEERS

Nine healthy volunteers (all male, mean age 29.8 years, age range from 23 to 47) participated with informed consent in the study, which was approved by the local ethics committee.

2.2 TASK DESIGN AND DATA ACQUISITION

The time delay between MR and PET scan sessions was different for each volunteer, which varied between 1-7 days.

2.2.1 Paradigm: Stimulation of the visual cortex was targeted with a block-design paradigm with alternating presentations of a flickering black/white polar checker board (grey background with a red fixation cross to keep the volunteers alert and minimize eye movement, 8 Hz) (stimulation) and a grey screen (rest condition). During each stimulation and rest condition block of 15 seconds, 5 whole-brain data sets ("dynamics") were acquired, resulting in a total of 80 scans.

2.2.2 fMRI/fQSM: Gradient-echo-EPI (FA = 90^{o}, TR = 3s, TE = 35ms, reconstructed voxel volume = 1.8 x 1.8 x 4 mm^3, matrix size: 128 x 128 x 30, number of time points: 80) images were acquired in axial orientation on a 3T MR system (Ingenia, Philips Healthcare, Best, The Netherlands), SENSE acceleration factor = 1.8, receive bandwidth (Hz/pixel) = 2035. T1-weighted (anatomical) images (3D Turbo-Field-Echo sequence, TE = 4.22ms, TR = 9.09 ms, FA = 8°, acquired in sagittal orientation, voxel size: 0.43 x 0.43 x 0.9 mm^3, matrix size: 560 x 560 x 200) were acquired for anatomical reference.

2.2.3 PET: The regional CBF response to the stimulus described above was also measured in the same volunteers using sequential O-15-water PET. The baseline condition was presented continuously for 5 min during the first imaging session. 10 min later the stimulus condition was presented for 5 min during a second imaging session. The baseline/stimulus conditions were started 1 min before O-15-water infusion. Dynamic PET images (18 x 10 s) were acquired in 3D mode on a full ring PET/CT scanner (PET/CT Discovery STE, GE Healthcare, Waukesha, MI, USA) and subsequently corrected for attenuation and scatter by an algorithm based on the

corresponding CT (120 kV/80 mA). A 3D Fourier rebinning filtered back projection algorithm was applied for image reconstruction. The 128 x 128 x 47 matrix resulted in a spatial resolution of 2.34 x 2.34 x 3.27 mm3 (voxel size). An automatic injection device administered 600 MBq of [15O]-water intravenously. During PET imaging the tracer activity in arterial blood was measured continuously using an automatic blood sampling device (swisstrace twilite, swisstrace, Menzingen, Switzerland). Arterial blood data was used as the input function for parametric maps of CBF (ml/min/100g), which were generated using a 1-tissue compartment model with look-up table approach (Alpert et al., 1984; Meyer, 1989) in PMOD (PXMOD tool, version 3.5, PMOD Technologies Ltd., Zurich, Switzerland). Individual activation maps were generated by subtraction of stimulation and baseline images after 3D spatial filtering (10 mm Gaussian) and the group-wise activation was assessed using SPM12.

2.3 MR DATA PROCESSING

2.3.1 QSM reconstruction

The post-processing is summarized in **Figure 1**. Dicom images with manufacturer-provided reconstructions of real and imaginary data were obtained from the scanner and used for post-processing. QSM reconstruction algorithms were based on custom Python routines (Python Software Foundation. Python Language Reference, version 2.7.).

The Laplacian of the unwrapped phase data, $L(WPI)$, was estimated from the wrapped phase information (Schofield and Zhu, 2003), WPI_w according to Eq. [2]

$$L(WPI) = cos(WPI_w) \times L\big(sin(WPI_w)\big) - sin(WPI_w) \times L\big(cos(WPI_w)\big), \qquad [2]$$

where "×" symbols denote an element-wise multiplication, and L is the smallest discrete Laplace operator (Schweser et al., 2013). A whole-brain binary mask was obtained from the magnitude data with the BET function (FSL (Jenkinson et al., 2012)), and multiplied with the $L(WPI)$ map after erosion (2-3 pixels), in order to reduce artifacts arising from the convolution step near the edges of the brain. The masked Laplacian of the unwrapped phase was subject to deconvolution in the Fourier domain, to obtain unwrapped and background-field corrected phase map (P_{corr}). For

functional analysis of the corrected phase data, the minimum phase value across the whole time series was subtracted from all phase data. The corresponding data is referred to as fPHASE.

Elements of the data matrix in Fourier space where absolute values of the corresponding elements in $|FT(l)|$, "l" being the kernel of the Laplace operator "L", were smaller than 0.2 were set to zero, to avoid division by zero and noise amplification. A map estimating local magnetic field differences, in ppb, was obtained by scaling the phase per echo time with the inverse of the gyromagnetic ratio, γ, the nominal field strength, B_0, and the echo-time, TE. Maps of local susceptibility differences, ΔX, in ppb, were calculated as (Marques, 2005):

$$\Delta X = FT^{-1} FT\,(-P_{corr}/(\gamma B_0 TE))/g, \qquad [3]$$

applying a variant of threshold-based k-space division (Özbay et al., 2015b) and with the filter g, in Fourier space, defined by $g = \frac{1}{3} - \frac{k_z^2}{k^2}, k^2 = k_x^2 + k_y^2 + k_z^2$. The symbol k_z denotes the k-component aligned with the main magnetic field. The processing was repeated for each 3D frame in the 4D EPI time-series phase data. For further analysis, the sign of the quantitative susceptibility data was inverted, and the minimum value across the whole time series was subtracted. The resulting non-negative data was compatible with a processing with the SPM12 software (Friston et al., 1995). The inverted and shifted time-series quantitative susceptibility data is referred as "*fQSM*" data throughout the manuscript.

2.3.2 Functional preprocessing

2.3.2.1 *MRI data*

The proposed pipeline is illustrated in **Figure-1**. The 4D magnitude data was masked using the same eroded mask as in the QSM reconstruction pipeline. The fPHASE and fQSM data were temporally band-pass filtered using the "fslmaths -bptf" function of FSL (Jenkinson et al., 2012),with a band-pass window for frequencies between ~0.03 and ~0.1 Hz. The remaining preprocessing was done with the Statistical Parametric Mapping (SPM) software (Friston et al., 1995), version SPM12 (http://www.fil.ion.ucl.ac.uk/spm/software/spm12/). The magnitude data was registered to the T1w data and the corresponding affine transformation was also applied to

both fPHASE and fQSM data. Following co-registration, fPHASE, fQSM and fMRI data were resliced. A step of an additional manual masking was necessary for the first two, to exclude regions with obviously distorted signal near air-tissue interfaces, i.e. near the frontal and aural cavities. All functional data were normalized to MNI space, with an isotropic resolution of 1 mm, and 183x219x183 voxels. fQSM and fMRI then spatially smoothed with a 3D Gaussian kernel with 3.5 x 3.5 x 3.5 mm^3 Gaussian smoothing. Additionally, fPHASE and fQSM analyses were repeated with a relatively small half-maximum full width of 1 x 1 x $1mm^3$ ($fQSM_{1.0}$, $fPHASE_{1.0}$) (**Fig.2**).

2.3.2.2 *PET data*

The PET data were pre-processed with the PMOD software. Stimulation and baseline images were smoothed with 1mm Gaussian kernel, and registered to the SPM-based brain (MNI) template with final isotropic resolution of 1mm, and 183 x 219 x 183 voxels. Registered maps were normalized with respect to the cerebellum, and smoothed with 10 mm Gaussian kernel.

2.3.2 Functional Data Analyses

2.3.2.1 *GLM Subject Level Analyses*

The pre-processed fMRI, fQSM, $fQSM_{1.0}$ and $fPHASE_{1.0}$ data were subject to General-Linear-Model (GLM) analyses using the SPM12 toolbox (SPM analysis toolbox). A combination of the canonical Hemodynamic Response Function and its derivatives with respect to time and dispersion was used as the basis function. The output of the GLM analysis, which includes the information of task paradigm and hemodynamic response function, is used as the reference function for temporal correlation with the ICA results.

2.3.2.2 *ICA Subject and Group Level Analyses*

The pre-processed functional data were analyzed using a spatial-domain ICA algorithm (FAST ICA) of the GIFT toolbox (Calhoun, 2004). The fMRI, fQSM, $fQSM_{1.0}$ and $fPHASE_{1.0}$ time-series data were all de-composed into 11 components, for each of which GIFT yielded ICA component maps, "*z*-score maps", as output. The thresholded map (*z*-score > 2.0 (McKeown et al., 1998)) of

the fQSM signal component that correlated best with the stimulation paradigm (highest Pearson correlation coefficient with the reference function) was overlaid on T1w images (**Fig. 3**). Exemplary time-courses of the corresponding components in the fQSM and fMRI analyses are shown in **Figure 3**. The algorithm of the GIFT toolbox was used for the group-level IC analyses of fQSM and fMRI data as well. The overlays of thresholded *z*-score maps (*z*-score > 1.0) from both visual components are given in **Figure 4**.

2.3.2.3 *PET Subject and Group Level Activation Maps*

For subject level analysis, the PET derived baseline CBF maps were subtracted from CBF maps acquired during stimulation and the results were overlaid on the T1w images (**Fig. 3**). Group-level *t*-score maps were calculated via Student's t-test (for paired samples) in SPM12 (SPM analysis toolbox) (**Fig.4**).

2.3.3 Volume of interest (VOI) analyses

Three volumes of interest (VOI) were used for subject-level numerical comparisons. The first VOI covered the whole visual area (VOI_{occ_lobe}) according to Hammer's atlas (Hammers et al., 2003) and was automatically segmented in the T1w image using PMOD. The second VOI (VOI_{veins}) included the largest apparent draining veins in 5-6 slices within VOI_{occ_lobe} and was manually drawn using *FSLview* (Jenkinson et al., 2012). The third VOI, $VOI_{GM\_occ\_lobe}$ was obtained from automated grey-matter segmentation inside VOI_{occ_lobe}, using FSL (Jenkinson et al., 2012). Exemplary outlines of VOI_{veins} are shown in **Figure 3b)**. The three VOIs were placed (copied) at exactly identical location to all MR-based *z*-score maps. For each VOI, *z*-score mean and standard deviations and the numbers of activated voxels (*N*), i.e., voxels with *z*-scores above a pre-defined threshold (*z*-score > 2.0) were determined. The percentages of activated voxels in $VOI_{GM\_occ\_lobe}$ and VOI_{veins} were determined, in relation to the whole of VOI_{occ_lobe}, and to the parts of VOI_{occ_lobe} in the slices also covered by VOI_{veins} ($VOI_{occ\_lobe\_selected}$), respectively, and compared between fQSM and fMRI. Means and standard deviations of *z*-scores in occipital-lobe voxels commonly activated in both fMRI and fQSM were also calculated. The results of these analyses of voxels

with positive *z-scores* are presented in **Tables 1 and 2**, including p-values from statistical comparisons (Wilcoxon test) between fQSM and fMRI. The threshold for significance was corrected for multiple-comparisons. Finally, numbers of voxels with *z*-scores below a pre-defined negative threshold (*z*-score < -2.0) were counted and summarized in **Table-3**.

2.3.4 Simulation Study

The magnetic-field offset around a homogeneous cylinder with a higher magnetic susceptibility than its surroundings was simulated by convolution of a discrete numerical phantom with the dipolar kernel *g*, as defined in the paragraph "QSM reconstruction" above. The phantom voxels were isotropic with a length of 0.3 times the cylinder's diameter. The phantom was binary in that voxels mostly inside the cylinder were set to a magnetic-susceptibility offset of 1 ppb, and all other voxels to a susceptibility offset of 0 ppb. The simulation was repeated with the cylinder long axis aligned with a homogeneous magnetic field of 3 Tesla and in the transverse plane.

3. RESULTS

3.1 fQSM: 4D EPI dynamic QSM reconstruction

The data of all volunteers were successfully processed. The pipeline with magnitude, raw phase and fQSM images is illustrated in **Figure 1**. An exemplary QSM image is shown in **Figure 3(b),** demonstrating that due to the sign-inversion of the susceptibility data, veins are depicted darker than the surrounding tissue, despite their higher susceptibility.

3.2 Simulation

Simulated magnetic-field offset maps are shown in (**Fig. 5**) along with in-vivo axial and sagittal slices of corrected phase maps and *z*-score maps of fMRI, $fPHASE_{1.0}$ and $fQSM_{1.0}$ that are thought to closely correspond to the simulations.

3.3 Functional analysis

3.3.1 Subject-level analysis

Figure 3 shows an exemplary subject-level PET derived activation map, and *z*-score maps of the paradigm-related component in fQSM ($|z\text{-score}| > 2.0$) and fMRI ($z\text{-score} > 2.0$) analyses. For this specific subject (subject number: 7), the ratio of number of activated voxels within VOI_{veins} *vs.* $VOI_{occ\_lobe\_selected}$ was 69 % for fQSM, and 32 % for fMRI. In **Figure 5** the simulated magnetic-field distribution in and around a cylinder aligned perpendicular to the main magnetic field is compared to functional parametric *z*-score maps in the region of large veins, roughly oriented in an axial plane and perpendicular to the main magnetic field. **Figure 2** shows additional adjacent *z*-score maps of the paradigm related components of fMRI, fQSM, $fQSM_{1.0}$ and $fPHASE_{1.0}$ data of the same volunteer, together with exemplary T1w slices and with a susceptibility map reconstructed from a single dynamic (QSM-EPI).

The regions indicating activation in fQSM, while roughly located in similar areas; do not entirely match with those in fMRI and in PET. In addition, strong fMRI correlations are predominantly positive, while fQSM showed both positive and negative correlations and *z*-scores. The areas of positive and negative correlation in the immediate neighborhood of the vein resemble the structure

of the phase- and field dipole before the dipolar-inversion step during the QSM processing, while such a phase-dipole is not really visible and appears quite successfully resolved by the dipolar inversion when considering the QSM-EPI data of a single dynamic.

3.3.2 Group-level analysis

Activation maps highlighted volumes of activation in the expected regions of visual cortex for fQSM, fMRI and PET data, compare **Figure 4**. The z_score thresholds were manually optimized for visualization and were 1.0 for MR-contrasts, fQSM and fMRI. The corresponding volumes of paradigm-activated tissue were, upon visual comparison, smaller for the fQSM than for the fMRI and PET data.

3.4 Volume of Interest (VOI) analysis

Tables 1-2 list the numbers of activated voxels (z-score > 2.0) within VOI_{occ_lobe}, $VOI_{GM\_occ\_lobe}$ and VOI_{veins}, and their ratios, as measured in each volunteer and in fMRI and fQSM data. Last rows of **Table 1** gives the average number of activated voxels over all volunteers for $fQSM_{1.0}$ data. The mean number of commonly activated voxels, N_{common} in VOI_{occ_lobe} and in fQSM and fMRI was 4375 ± 1211 or the ratio of these common voxels with respect to the number of voxels in fQSM, $N_{\text{common}} / N_{,}$ was 0.39 ± 0.11 (last two columns in VOI_{occ_lobe}, **Table 1**). In all three VOI's the numbers of activated voxels were lower for fQSM than for fMRI, with the strongest reduction by 65.9 % in $VOI_{GM\_occ\_lobe}$ (17114 ± 3373 versus 5832 ± 1202, $p < 0.00005$), a strong reduction by 63.6 % in VOI_{occ_lobe} (31113 ± 6111 versus 11301 ± 1845, $p < 0.00005$) and the smallest reduction by 28.1 % in, VOI_{veins} (1620 ± 613 versus 1164 ± 383, $p < 0.2$). In contrast, the ratio of number of activated voxels within VOI_{veins} *vs.* $VOI_{occ\_lobe\_selected}$ was significantly higher (0.57 ± 0.13) for fQSM than for fMRI (0.34 ± 0.10) ($p < 0.0007$), whereas, the ratios of number of voxels activated in $VOI_{GM\_occ\_lobe}$ *vs.* VOI_{occ_lobe} were 0.52 ± 0.08 for fQSM and 0.55 ± 0.02 for fMRI and not statistically significantly different.

The proportions of voxels with a large negative *z*-score (< -2.0), in relation to all apparently activated voxels (|*z*-score| > 2.0) were 43, 44, and 23 % for VOI_{occ_lobe}, $VOI_{GM\_occ\_lobe}$, and VOI_{veins}, respectively, in fQSM, and 4, 4, and < 1 % in fMRI (**Tables 1 - 3**).

The mean *z*-scores over all volunteers for VOI_{occ_lobe} and $VOI_{GM\_occ\_lobe}$ were higher in fMRI (VOI_{occ_lobe}: 4.30 ± 0.27, $VOI_{GM\_occ\_lobe}$; 4.30 ± 0.27) than for fQSM (VOI_{occ_lobe}: 3.52 ± 0.40, $VOI_{GM\_occ\_lobe}$: 3.51 ±0.37) (VOI_{occ_lobe}: $p < 0.0005$, $VOI_{GM\_occ\_lobe}$: $p < 0.0002$), while in VOI_{veins} the average *z*-scores of activated voxel were comparable (fMRI: 4.11 ± 0.96, fQSM: 4.09 ± 0.85) and the difference was not significant ($p < 1.0$). The mean *z*-score in the occipital-lobe voxels that were commonly activated both in fQSM and fMRI was higher in fMRI (4.46 ± 0.71) than in fQSM (3.68 ± 0.44; **Tables 1-2**).

In the group-level analysis of the co-registered data sets with identical nominal voxel size (**Figure 4**) the numbers of activated (*z*-score > 1.0) VOI_{occ_lobe} voxels were 7846 and 27601 for fQSM and fMRI and 22267 for PET ($p < 0.001$, $T > 4.5$). Their mean values and standard deviations were 1.82 ± 0.88 for fQSM, 2.58 ± 1.54 fMRI (both *z*-scores), and 6.83 ± 1.83 for PET (*t*-score).

4. DISCUSSION

In this study, we used 4D phase data from a 3T clinical MR-scanner to reconstruct dynamic susceptibility distributions and map regions of brain-tissue susceptibility changes induced by a visual stimulus for neuronal activation. A successful exploitation of advanced fMRI tools for fQSM required only minor adaptions, in particular, a sign-inversion of the QSM data, and a subtraction of the minimum susceptibility value over the whole time series.

We could confirm that within prominent areas of positive fQSM correlations that lie inside PET- and fMRI activation regions, there was a good correlation between fQSM and fMRI signal time courses, i.e., consistent with previous reports on phase-data based fMRI (Hagberg and Tuzzi, 2014). For this comparison it should be kept in mind that the visual block paradigm was different for MRI and PET. The scanning protocol for O-15-water PET differed substantially from fMRI protocols. Each scan required 3 min of dynamic PET acquisition after a short infusion of O-15-water. Thus each condition (baseline and visual stimulation) covered the time required for whole brain data acquisition. O-15-water is the gold standard PET tracer for measurement of cerebral blood flow, and was used for functional activation studies before fMRI (Fox et al., 1984). O-15-water PET only takes about 3 min per scan, much less time compared to FDG-PET (Hurtig et al., 1994), and due to low radiation exposure (very short tracer half-life) can be repeated several times in the same volunteer. 18F-FDG PET measures glucose metabolism, which is closely linked to cerebral blood flow, but requires about 1 hour of tracer uptake for reliable quantitative analysis, hence in the current study O-15-water was used as a tracer. Although stimulation-induced changes of cerebral blood flow and BOLD MR signal potentially could reflect different phenomena, striking similarities between flow- and BOLD-defined areas of neuronal activation have been reported in functional studies at very high field (Bause et al., 2016; Detre and Wang, 2002). In agreement with previous studies (Balla et al., 2014; Bianciardi et al., 2014; Chen and Calhoun, 2015a), we also confirm that the QSM-specific phase processing, with the application of Laplacian-like high-pass filters, may quite successfully alleviate a range of problems with long-

range spatial and temporal phase variations (Özbay et al., 2014b). While, in general, lower numbers of activated voxels with lower mean *z*-scores were found in fQSM than in fMRI of the same data, using identical thresholds, the fraction of activated voxels in VOIs closely restricted to large veins with a stimulation-induced venous oxygen saturation (SvO2) change and their mean *z*-score were indeed higher in fQSM than in fMRI, indicating that QSM generally does a reasonable job at mapping stimulation-induced non-local field- and phase-changes back to the vein as the underlying source of the change. Hypothetically, this promises a reduced potential for tissue regions false positively being associated with neuronal activation and a better localization of large-vessel BOLD effects in fQSM than in gradient-echo based fMRI. Nevertheless, the fraction of activated voxels in gray-matter segments of larger VOI's was comparable in fQSM and fMRI, suggesting, that fQSM may still detect gray-matter activation in tissues without larger venous vessels. Finally, we believe that some of our results may be instrumental for an improved understanding of the activation patterns in fQSM, compared below.

So far, fQSM studies mainly reported single-subject GLM results, c.f. a recent comprehensive study that compared findings obtained with various QSM processing techniques and with highly resolved 7T data (Balla et al., 2014), or a volunteer study (Chen et al., 2013) on a 3-Tesla system. Both studies found that, although there are common patterns of activated regions in fQSM and fMRI, the exact locations with the highest *z*-scores may differ in the two evaluations. They (Balla et al., 2014; Chen and Calhoun, 2015a; Chen et al., 2013) also found areas that significantly and negatively correlated with the stimulation time course that were clearly more prominent in fQSM than in fMRI. Although the projected benefits of fQSM are significant, the activation patterns are not yet well understood and further validation and reproducibility studies are required. One of the studies (Balla et al., 2014) specifically directed future attention to tissue regions close to larger veins, with non-local field- and phase-interference. In our study we consistently observed bi-lateral draining veins with a significant response to the visual stimulation paradigm, which allowed a closer examination of the corresponding effects. In the fQSM parametric maps, obtained

after sign-inversion of the susceptibility maps, the inside of the veins, which were roughly oriented orthogonal to the direction of the main magnetic field, showed strong positive correlation with the stimulus, just as in fMRI. In contrast, the immediate surroundings of the vein correlated either positively (same sign as interior of vein, as seen in image planes containing the vein and oriented perpendicular to the main-field direction, compare **Fig. 5**) or negatively (opposite sign as interior of vein, as seen in image planes that contain both the vein and the vector of the main magnetic field, compare **Fig. 3**). Similar observations, albeit with lower *z*-scores, could also be made in parametric maps derived from the phase images, compare **Figs 2, 5**. Both observations are consistent with results reported by (Balla et al., 2014).

In summary, the immediate surroundings of large veins with stimulus-induced SvO2 increase and aligned orthogonally to the field, showed activation patterns that would be expected for these regions if the field- and phase-dipole induced by susceptibility changes inside the vein was incompletely resolved by the QSM processing step of dipolar inversion. The pattern was more clearly visualized in fQSM *z*-score map than in fPHASE z-score maps. The hypothetical deficiencies of the inversion were too small to be visualized in a single QSM dynamic data frame, but appear to have been picked up by the statistical mapping process. It is important to note that this phenomenology was independently observed for various QSM processing algorithms (Balla et al., 2014) and acquisition parameters (Balla et al., 2014; Chen and Calhoun, 2015a), as well as in GLM and ICA analysis (Balla et al., 2014; Chen and Calhoun, 2015a), and, thus, does not seem to be an artifact of our particular processing pipeline. While possible starting points for an analysis of and an explanation of these observations seem outlined by the above detailed phenomenological description, they clearly are beyond the scope of the current study.

In a recent 7T-fQSM study with data of high SNR and spatial resolution (Balla et al., 2014), any spatial smoothing of fQSM data was avoided, due to its large effect on parameter estimates. In our 3T-study, the fQSM data was smoothed (Gaussian 3.5-mm kernel) as fMRI, to improve the statistical robustness, and to allow meaningful comparisons with thresholding and voxel counts for

MR data. As already previously shown (Özbay et al., 2015a) a temporal band-pass filter was required in fQSM processing for a clear identification of the independent component that reflects paradigm-induced temporal changes with largest likelihood, whereas the temporal filter was not necessary in fMRI processing. In an isolated test (data not shown), the temporal band-pass filtering of the fMRI data of a single volunteer consistently reduced the number of voxels in all evaluated VOIs. However, the change was less than 5% and the voxel-number fractions, as reported in the tables, were virtually unchanged. Thus, it seems unlikely that this difference in the data processing may have induced a sufficiently large bias to change the conclusions. Brain mask erosion, here by 2-3 pixels with a 4 mm slice thickness, is an inherent limitation to current state-of-the-art QSM processing that potentially results in the loss of important parts of the visual cortex. In an attempt to not unnecessarily distort relative voxel counts the same mask was applied in the processing of all fQSM and fMRI data.

Probing brain activity by means of fQSM is highly attractive for fundamental as well as practical reasons. Among the latter is the fact that, in principle, any fMRI scan can yield phase data that can be subject to QSM processing and provide complementary functional information without additional scan time. Among the former are the prospect that the susceptibility measured in any given voxel, beyond being quantitatively comparable across acquisitions with different parameters, scanners, field-strengths and institutions, may more truthfully and directly report on a meaningful parameter of local physiology in the voxel, less disturbed by non-local interference than a T2*-weighted signal intensity, as in traditional fMRI, which dominantly reflects changes of magnetic-field gradients.

In conclusion, as we demonstrated here, fQSM can be implemented to exploit well-established fMRI tools, profiting from large efforts put into optimization of fMRI. Nevertheless, it seems clear that the issue of the consistently reported mixture of positive and negative correlation patterns needs to be solved before fQSM can fully live up to its projected potential. We hope that the detailed phenomenological description provided in this manuscript will contribute to this progress.

It can be speculated that fQSM and QSM may prove particularly useful, e.g., in future studies with an interest in layer-specific functional information (Koopmans et al., 2011), in attempts to focus on vascular components and venography (Fan et al., 2014) of neuronally activated regions, or quantification of tissue oxygenation (Özbay et al., 2015b) and cerebral metabolic rate of oxygen consumption (Zhang et al., 2015). Such studies may also benefit from the recent achievements in accelerating the QSM processing (Bilgic et al., 2014; Langkammer et al., 2015).

Figures:

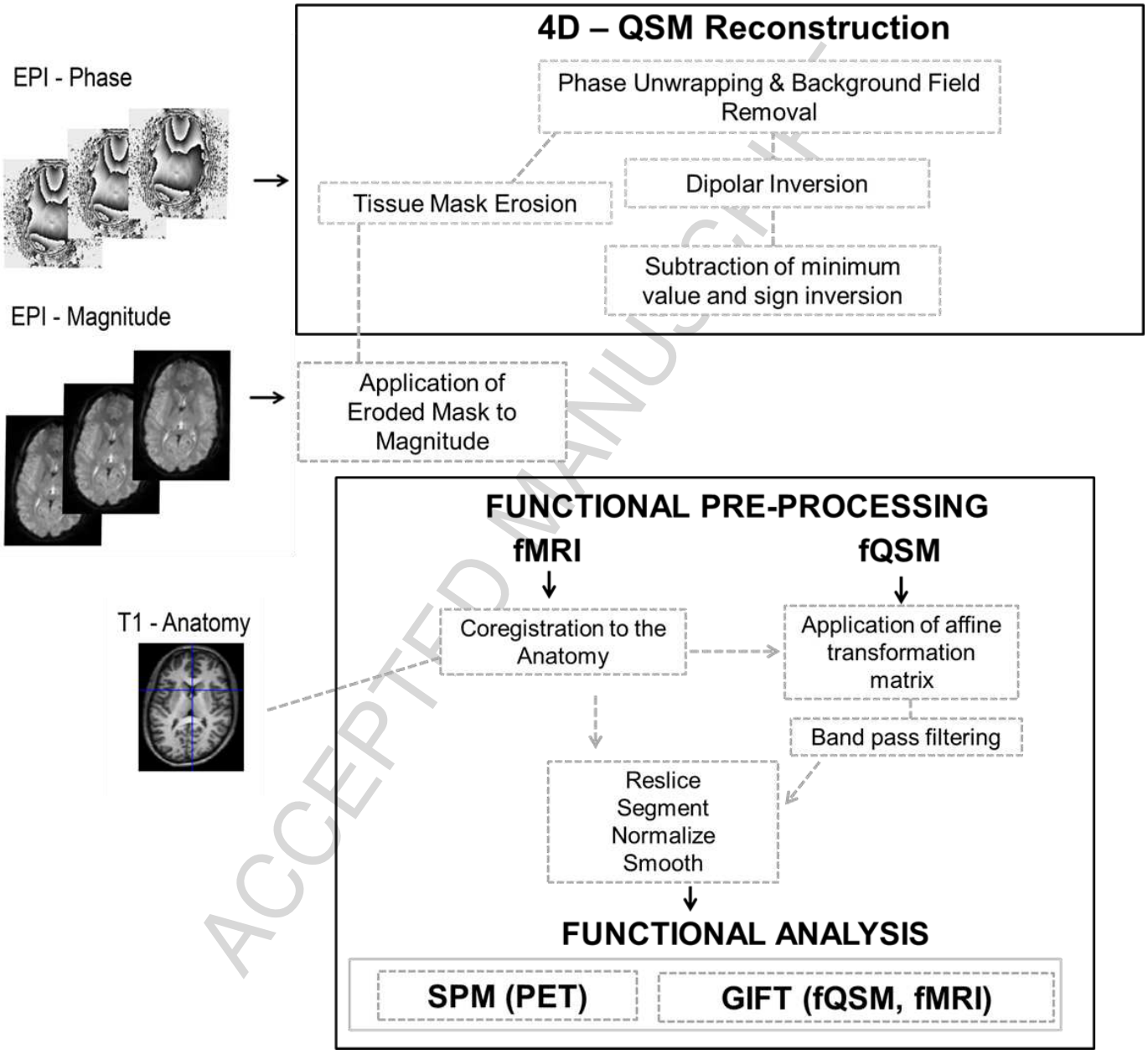

Figure 1: Pipeline of fQSM and fMRI processing. QSM post-processing from 4D phase data (up), and functional analysis of both Magnitude, fQSM and PET data (bottom).

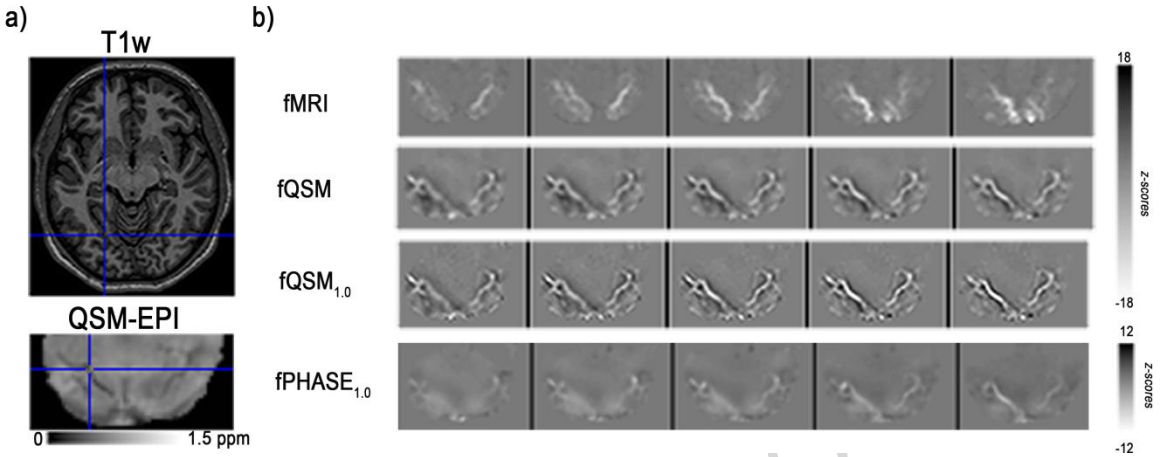

Figure 2: a) (left) T1w and QSM-EPI (sign inverted, and shifted susceptibility map) image of slice number 64, b) Exemplary contiguous axial slices (slice numbers: 55, 57, 59, 61, 63) of z_score maps: fMRI, fQSM, $fQSM_{1.0}$ and $fPHASE_{1.0}$, (subject number=9). For sign conventions compare caption to **Fig. 5**. Note that in the fQSM maps the veins are brightly depicted in more adjacent slices than in the fMRI map, likely due to the phase-dipole resembling geometry of the areas with significant correlation.

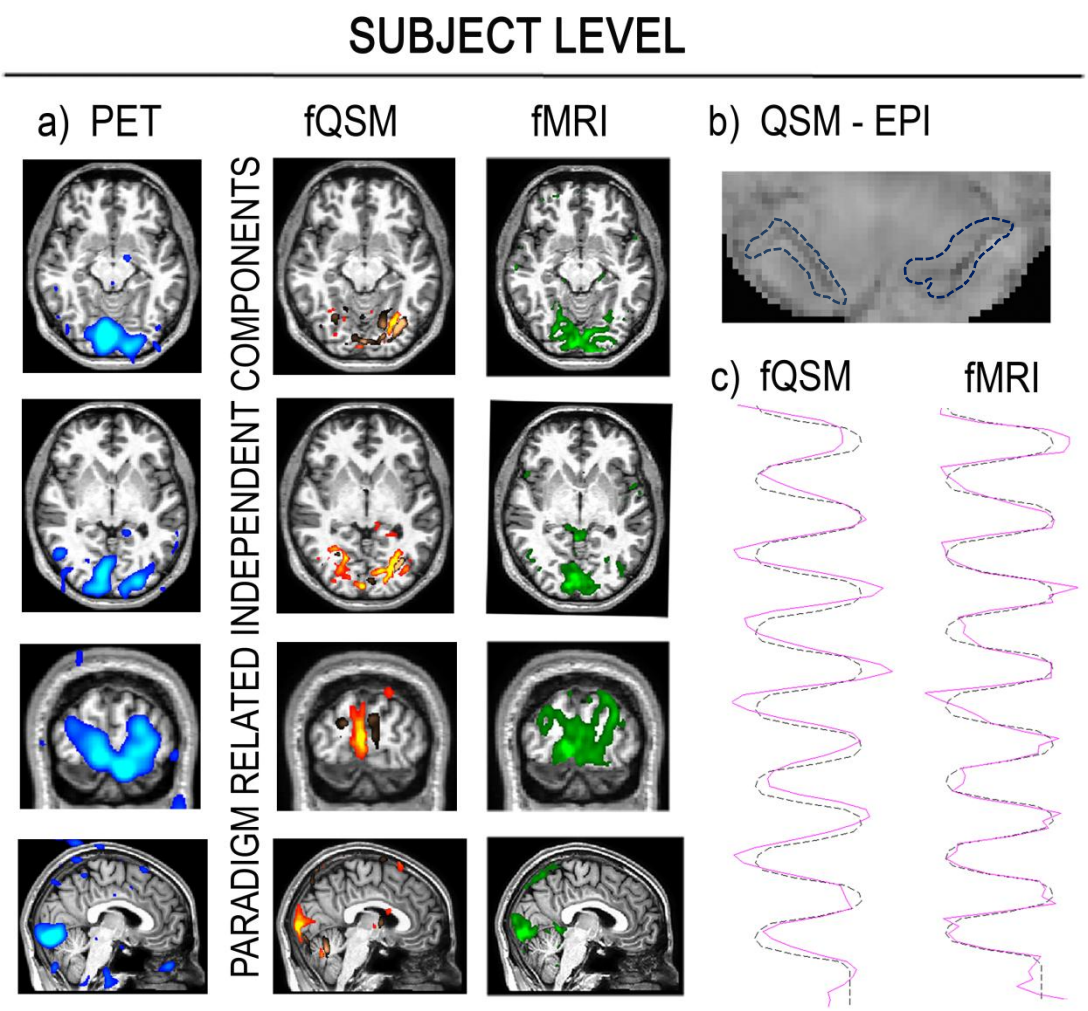

Figure 3: a) Exemplary single-subject CBF-based activation maps derived by subtracting post-processed baseline from stimuli PET images (**blue**, left), *z*-score maps from the ICA single-subject fQSM (**orange** (*z*-score > 2.0), **copper** (*z*-score < -2.0), middle) and fMRI (**green** (*z*-score > 2.0), right) analyses (subject number=7, visual activated regions displayed over an anatomical T1w image), b) single slice of QSM-EPI data (sign-inverted and shifted susceptibility map) from the same volunteer, showing an exemplary placing of volumes of interests, VOI_{veins} (**blue**, bi-lateral veins) c) temporal change of paradigm related independent components (**pink**, continuous line) of fQSM (left) and fMRI (right) (black dotted background, reference function).

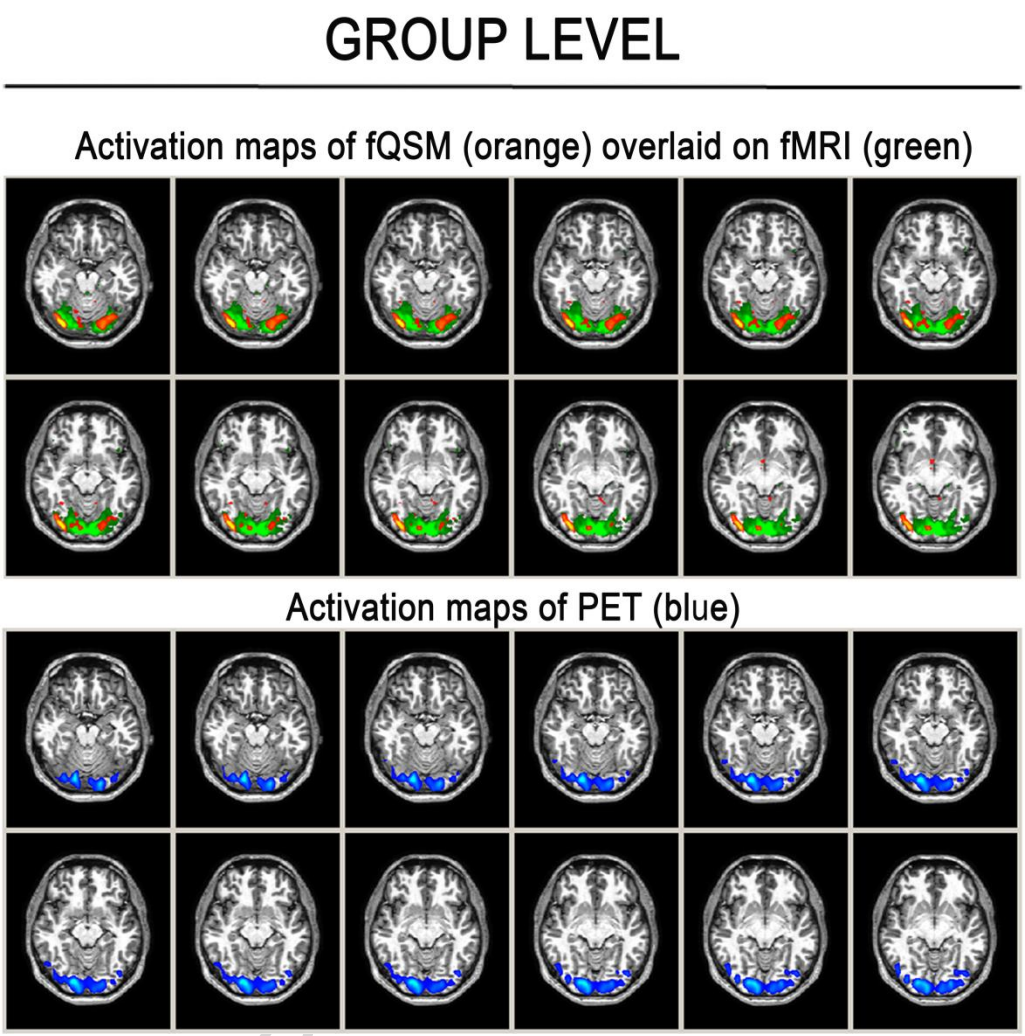

Figure 4: Group level analysis: *z*-score maps of fQSM (*z*-score > 1.0, **orange**), overlaid on *z*-score maps of fMRI (*z*-score > 1.0, **green**)(top), and *t*-score maps of PET ($p < 0.001$, **blue**) (bottom) (number of subjects=9).

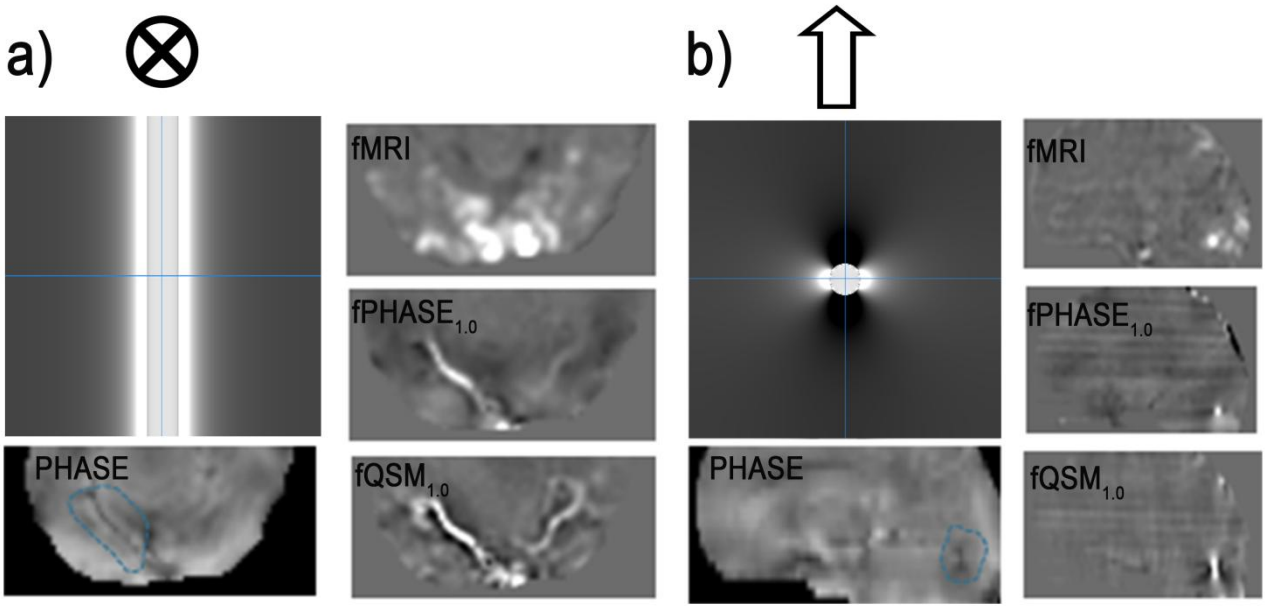

Figure 5: Left columns, a-b), top: simulated sign-inverted magnetic-field distribution in and around a cylinder (vein) oriented perpendicular to the main magnetic field, whose direction is indicated by the circled cross (a) and the arrow (b), respectively, and bottom: trans-axial, background-corrected phase maps, range [-0.7 to 4.3] rad. Right columns, a-b), top to bottom: fMRI, $fPHASE_{1.0}$ and $fQSM_{1.0}$ *z*-score maps, respectively; fMRI: *z*-score range [-5.8 to 10], $fPHASE_{1.0}$: [-4.6 to 7], $fQSM_{1.0}$: [-7.2 to 10]). The QSM data were sign-inverted before parametric mapping, thus bright areas in all statistical parametric maps indicate a positive correlation with a stimulation-induced periodic SvO2 increase and concomitant susceptibility decrease. Experimental data stem from subject number 9.

Tables

Table 1 Numbers of activated voxels (z-score > 2.0) in volumes of interest in fQSM data[a,b,c,d,e]

fQSM	**VOI_{occ_lobe}**							**$VOI_{GM\_occ\_lobe}$**				**VOI_{veins}**			
Volunteer	N [*]	z-scores		z-scores (common voxels)		N_{common}	N_{common} / N	N [*]	f	z-scores		N	f [***]	z-scores	
		mean [**]	SD [**]	mean	SD					Mean [***]	SD			mean	SD
1	11112	3.83	2.06	3.73	1.68	4949	0.44	6288	0.56	3.88	3.01	1259	0.65	4.64	1.9
2	10621	2.95	0.96	3.12	0.99	5157	0.48	4994	0.47	3.01	0.96	988	0.55	3.49	1.07
3	11626	3.42	1.32	3.23	1.12	4277	0.37	6208	0.53	3.43	1.29	1829	0.42	3.92	1.5
4	10960	3.50	1.59	3.64	1.68	5808	0.53	6813	0.62	3.42	1.49	1238	0.74	3.60	1.46
5	7667	3.12	1.36	3.62	1.78	2248	0.29	4307	0.56	3.13	1.44	360	0.4	3.69	1.47
6	11466	3.23	1.62	3.35	1.85	5423	0.47	6358	0.55	3.15	1.55	1225	0.53	3.03	0.83
7	12938	4.22	2.53	4.17	2.05	2646	0.2	4270	0.33	4.04	2.2	1218	0.69	4.57	2.63
8	14531	3.89	2.23	4.49	2.61	4223	0.29	7901	0.54	3.86	2.2	1052	0.44	5.93	3.45
9	10878	3.55	1.59	3.75	1.67	4626	0.42	5351	0.49	3.64	1.63	1306	0.67	3.98	1.96
Mean	11311	3.52	1.7	3.68	1.71	4373	0.39	5832	0.52	3.51	1.75	1164	0.57	4.09	1.81
SD	1845	0.4	0.49	0.44	0.48	1209	0.11	1202	0.08	0.37	0.62	383	0.13	0.85	0.81
$fQSM_{1.0}$															
Mean	9882	3.87	2.18	3.7	2.13	4128	0.42	5112	0.52	3.86	2.11	1155	0.6	4.69	2.5
SD	1909	0.46	0.58	0.5	0.49	1106	0.11	1162	0.07	0.47	0.56	350	0.11	1.1	1.1

[a] Volumes of interest: VOI_{occ_lobe}: whole occipital lobe, $VOI_{GM\_occ\_lobe}$: grey matter within VOI_{occ_lobe}, VOI_{veins}: large veins

[b] N: number of activated voxels in the volume of interest.

[c] N_{common}: number of voxels in the volume of interest activated in both fQSM and fMRI.

[d] f: ratio between N in the volume of interest and N in the relevant parts of VOI_{occ_lobe}, compare text.

[e] Stars and symbols indicate statistically significant differences between fQSM and fMRI:

[*]: $p < 0.00005$, [**]: $p < 0.003$, [***]: $p < 0.0007$.

Table 2 Numbers of activated voxels (z-score > 2.0) in volumes of interest in fMRI data[a,b,c].

fMRI	**VOI_{occ_lobe}**					**$VOI_{GM\_occ\_lobe}$**				**VOI_{veins}**			
Volunteer	***N***	***z*-scores**		***z*-scores** *(common voxels)*		***N***	***f***	***z*-scores**		***N***	***f***	***z*-scores**	
		mean	SD	mean	SD			mean	SD			mean	SD
1	27400	4.59	2.89	5.85	3.62	15367	0.56	4.70	3.00	1887	0.37	6.30	3.22
2	43932	3.97	1.92	4.13	1.90	23333	0.53	3.90	1.89	2213	0.3	4.15	1.67
3	27705	4.29	2.67	3.83	1.79	14704	0.53	4.23	2.56	951	0.23	3.91	1.63
4	37942	3.96	2.11	3.88	2.00	21463	0.56	4.02	2.09	2744	0.58	3.89	1.71
5	30669	4.20	2.29	3.87	1.77	16931	0.55	4.21	2.3	1207	0.27	4.26	1.43
6	28014	4.54	2.66	4.58	2.36	15969	0.57	4.60	2.78	1663	0.35	4.41	2.13
7	31428	4.02	2.19	4.18	2.50	17787	0.57	4.14	2.3	1568	0.31	3.42	1.47
8	24309	4.61	4.70	4.50	4.31	12473	0.51	4.30	4.29	785	0.35	2.76	0.63
9	28619	4.48	2.61	5.36	2.98	16001	0.56	4.56	2.66	1562	0.32	3.89	2.21
Mean	31113	4.30	2.67	4.46	2.58	17114	0.55	4.30	2.65	1620	0.34	4.11	1.79
SD	6111	0.27	0.82	0.71	0.89	3373	0.02	0.27	0.7	613	0.10	0.96	0.7‘

[a] Volumes of interest: VOI_{occ_lobe}: whole occipital lobe, $VOI_{GM\_occ\_lobe}$: grey matter within VOI_{occ_lobe}, VOI_{veins}: large veins

[b] *N*: number of activated voxels in the volume of interest.

[c] *f*: ratio between *N* in the volume of interest and *N* in the relevant parts of VOI_{occ_lobe}, compare text.

Table 3 Numbers of activated voxels (z-score < -2.0) in volumes of interest in fQSM and fMRI data ($p < 0.001$).

Volunteer	fQSM			fMRI		
	VOI_{occ_lobe}	$VOI_{GM\_occ\_lobe}$	VOI_{veins}	VOI_{occ_lobe}	$VOI_{GM\_occ\_lobe}$	VOI_{veins}
1	8207	3640	241	312	137	0
2	8792	4265	213	467	169	0
3	5479	3443	28	2300	1100	0
4	7122	3518	397	390	135	0
5	6583	3660	303	1217	730	37
6	10744	5499	311	6063	2874	25
7	11842	6614	600	1413	674	2
8	9776	4984	378	191	27	0
9	9061	5250	738	639	305	0
Mean	8623	4541	357	1444	683	7
SD	2027	1109	210	1860	895	14

Acknowledgments

The authors thank Lars Kasper (IBT, ETH Zürich) for initial guidance with the SPM analysis. GW was partly supported by the CRPP Tumor Oxygenation grant (University of Zurich/University Hospital Zurich).

REFERENCES

Alpert, N.M., Eriksson, L., Chang, J.Y., Bergstrom, M., Litton, J.E., Correia, J.A., Bohm, C., Ackerman, R.H., Taveras, J.M., 1984. Strategy for the measurement of regional cerebral blood flow using short-lived tracers and emission tomography. J Cereb Blood Flow Metab 4, 28-34.

Arja, S.K., Feng, Z., Chen, Z., Caprihan, A., Kiehl, K.A., Adali, T., Calhoun, V.D., 2010. Changes in fMRI magnitude data and phase data observed in block-design and event-related tasks. Neuroimage 49, 3149-3160.

Balla, D.Z., Sanchez-Panchuelo, R.M., Wharton, S.J., Hagberg, G.E., Scheffler, K., Francis, S.T., Bowtell, R., 2014. Functional quantitative susceptibility mapping (fQSM). Neuroimage 100, 112-124.

Bause, J., Ehses, P., Mirkes, C., Shajan, G., Scheffler, K., Pohmann, R., 2016. Quantitative and functional pulsed arterial spin labeling in the human brain at 9.4 t. Magn Reson Med 75, 1054-1063.

Bianciardi, M., van Gelderen, P., Duyn, J.H., 2014. Investigation of BOLD fMRI resonance frequency shifts and quantitative susceptibility changes at 7 T. Hum Brain Mapp 35, 2191-2205.

Bilgic, B., Fan, A.P., Polimeni, J.R., Cauley, S.F., Bianciardi, M., Adalsteinsson, E., Wald, L.L., Setsompop, K., 2014. Fast quantitative susceptibility mapping with L1-regularization and automatic parameter selection. Magn Reson Med 72, 1444-1459.

Blockley, N.P., Griffeth, V.E., Simon, A.B., Buxton, R.B., 2013. A review of calibrated blood oxygenation level-dependent (BOLD) methods for the measurement of task-induced changes in brain oxygen metabolism. NMR Biomed 26, 987-1003.

Calhoun, V.C., 2004. Group ICA of fMRI Toolbox (GIFT). Available at: http://icatb.sourceforge.net.

Chen, Z., Calhoun, V., 2015a. Intrinsic functional brain mapping in reconstructed 4D magnetic susceptibility (chi) data space. J Neurosci Methods 241, 85-93.

Chen, Z., Calhoun, V., 2015b. Nonlinear magnitude and linear phase behaviors of T2* imaging: theoretical approximation and Monte Carlo simulation. Magn Reson Imaging 33, 390-400.

Chen, Z., Calhoun, V.D., 2011. Two pitfalls of BOLD fMRI magnitude-based neuroimage analysis: non-negativity and edge effect. J Neurosci Methods 199, 363-369.

Chen, Z., Liu, J., Calhoun, V.D., 2013. Susceptibility-based functional brain mapping by 3D deconvolution of an MR-phase activation map. J Neurosci Methods 216, 33-42.

Deh, K., Nguyen, T.D., Eskreis-Winkler, S., Prince, M.R., Spincemaille, P., Gauthier, S., Kovanlikaya, I., Zhang, Y., Wang, Y., 2015. Reproducibility of quantitative susceptibility mapping in the brain at two field strengths from two vendors. J Magn Reson Imaging.

Detre, J.A., Wang, J., 2002. Technical aspects and utility of fMRI using BOLD and ASL. Clin Neurophysiol 113, 621-634.

Fan, A.P., Bilgic, B., Gagnon, L., Witzel, T., Bhat, H., Rosen, B.R., Adalsteinsson, E., 2014. Quantitative oxygenation venography from MRI phase. Magn Reson Med 72, 149-159.

Fan, A.P., Schafer, A., Huber, L., Lampe, L., von Smuda, S., Moller, H.E., Villringer, A., Gauthier, C.J., 2016. Baseline oxygenation in the brain: Correlation between respiratory-calibration and susceptibility methods. Neuroimage 125, 920-931.

Fox, P.T., Mintun, M.A., Raichle, M.E., Herscovitch, P., 1984. A noninvasive approach to quantitative functional brain mapping with H2 (15)O and positron emission tomography. J Cereb Blood Flow Metab 4, 329-333.

Friston, K., Holmes, A., Worsley, K., Poline, J.B., Frith, C., Frackowiak, R., 1995. Statistical parametric maps in functional imaging: a general linear approach.
. Hum Brain Mapp 2.

Hagberg, G.E., Tuzzi, E., 2014. Phase Variations in fMRI Time Series Analysis: Friend or Foe? . Advanced Brain Neuroimaging Topics in Health and Disease - Methods and Applications, pp. 91-122

Hammers, A., Allom, R., Koepp, M.J., Free, S.L., Myers, R., Lemieux, L., Mitchell, T.N., Brooks, D.J., Duncan, J.S., 2003. Three-dimensional maximum probability atlas of the human brain, with particular reference to the temporal lobe. Hum Brain Mapp 19, 224-247.

Hurtig, R.R., Hichwa, R.D., O'Leary, D.S., Boles Ponto, L.L., Narayana, S., Watkins, G.L., Andreasen, N.C., 1994. Effects of timing and duration of cognitive activation in [15O]water PET studies. J Cereb Blood Flow Metab 14, 423-430.

Jenkinson, M., Beckmann, C.F., Behrens, T.E., Woolrich, M.W., Smith, S.M., 2012. FSL. Neuroimage 62, 782-790.

Koopmans, P.J., Barth, M., Orzada, S., Norris, D.G., 2011. Multi-echo fMRI of the cortical laminae in humans at 7 T. Neuroimage 56, 1276-1285.

Langkammer, C., Bredies, K., Poser, B.A., Barth, M., Reishofer, G., Fan, A.P., Bilgic, B., Fazekas, F., Mainero, C., Ropele, S., 2015. Fast quantitative susceptibility mapping using 3D EPI and total generalized variation. Neuroimage 111, 622-630.

Marques, J.P.B., R. , 2005. Application of a Fourier-based method for rapid calculation of field inhomogeneity due to spatial variation of magnetic susceptibility. Concepts Magn Reson B Magn Reson Eng 25, 14.

McKeown, M.J., Makeig, S., Brown, G.G., Jung, T.P., Kindermann, S.S., Bell, A.J., Sejnowski, T.J., 1998. Analysis of fMRI data by blind separation into independent spatial components. Hum Brain Mapp 6, 160-188.

Meyer, E., 1989. Simultaneous correction for tracer arrival delay and dispersion in CBF measurements by the H215O autoradiographic method and dynamic PET. J Nucl Med 30, 1069-1078.

Özbay, P., Rossi, C., Warnock, G., Kuhn, F., Akin, B., Prüssmann, K., Nanz, D., 2015a. Independent Component Analysis (ICA) of functional QSM. Proceedings of the 23rd Annual Meeting ISMRM, Toronto, 2015; 3932.

Özbay, P.S., Rossi, C., Kocian, R., Redle, M., Boss, A., Pruessmann, K.P., Nanz, D., 2015b. Effect of respiratory hyperoxic challenge on magnetic susceptibility in human brain assessed by quantitative susceptibility mapping (QSM). NMR Biomed 28(12),1688-1696.

Özbay, P.S., Rossi, R., Warnock, G., F., K., Pruessmann, K.P., Nanz, D., 2014a. Comparing Functional QSM and BOLD-fMRI by Statistical Parametric Mapping (SPM). 3rd Phase Contrast & QSM Workshop, Duke University, Durham, USA.

Özbay, P.S., Rossi, R., Warnock, G., Pruessmann, K.P., Nanz, D., 2014b. Does the Laplacian of functional MRI phase data allow a direct detection of brain activation? , Organization of Human Brain Mapping. Organization of Human Brain Mapping, Hamburg, Germany.

Özbay, P.S., Rossi, R., Warnock, G., Pruessmann, K.P., Nanz, D., 2014c. Functional Quantitative Susceptibility Mapping in Comparison with BOLD and PET. Proceedings of the Joint Annual Meeting ISMRM-ESMRMB, Milan, 2014; 3170.

Schofield, M.A., Zhu, Y., 2003. Fast phase unwrapping algorithm for interferometric applications. Opt Lett 28, 1194-1196.

Schweser, F., Deistung, A., Sommer, K., Reichenbach, J.R., 2013. Toward online reconstruction of quantitative susceptibility maps: superfast dipole inversion. Magn Reson Med 69, 1582-1594.

Shmueli, K., de Zwart, J.A., van Gelderen, P., Li, T.Q., Dodd, S.J., Duyn, J.H., 2009. Magnetic susceptibility mapping of brain tissue in vivo using MRI phase data. Magn Reson Med 62, 1510-1522.

SPM analysis toolbox, U., London, UK.

Sun, H., Wilman, A.H., 2015. Quantitative susceptibility mapping using single-shot echo-planar imaging. Magn Reson Med 73, 1932-1938.
Turner, R., 2002. How much cortex can a vein drain? Downstream dilution of activation-related cerebral blood oxygenation changes. Neuroimage 16, 1062-1067.
Wehrli, F.W., Fan, A.P., Rodgers, Z.B., Englund, E.K., Langham, M.C., 2016. Susceptibility-based time-resolved whole-organ and regional tissue oximetry. NMR Biomed doi: 10.1002/nbm.3495.
Zhang, J., Liu, T., Gupta, A., Spincemaille, P., Nguyen, T.D., Wang, Y., 2015. Quantitative mapping of cerebral metabolic rate of oxygen (CMRO2) using quantitative susceptibility mapping (QSM). Magn Reson Med 74, 945-952.

Graphical abstract

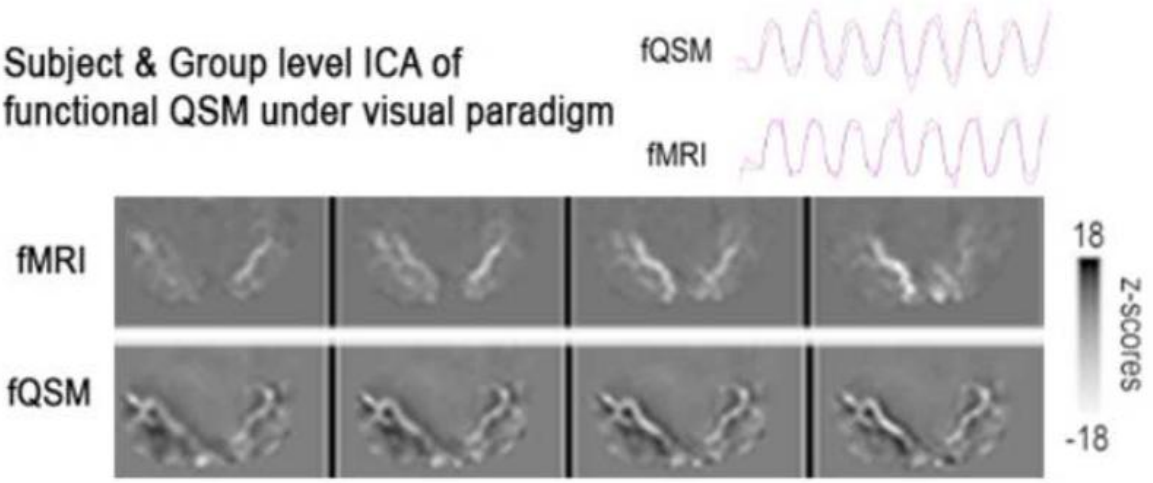

Highlights

- fQSM can map activated brain regions in response to visual stimulation at 3 T.
- fQSM localized a comparable fraction of activated voxels in grey matter as fMRI.
- fQSM localized a higher fraction of activated voxels in draining veins than fMRI.
- Some areas of apparent negative fQSM activation had no correlate in fMRI and PET.
- Their shape resembled large-vein field dipoles after incomplete dipolar inversion.